

Statistical Analysis of CFD Solutions from the Third AIAA Drag Prediction Workshop (Invited)

Joseph H. Morrison ^{*} and Michael J. Hemsch [†]
NASA Langley Research Center, Hampton, Virginia, 23681

The first AIAA Drag Prediction Workshop, held in June 2001, evaluated the results from an extensive N-version test of a collection of Reynolds-Averaged Navier-Stokes CFD codes. The code-to-code scatter was more than an order of magnitude larger than desired for design and experimental validation of cruise conditions for a subsonic transport configuration. The second AIAA Drag Prediction Workshop, held in June 2003, emphasized the determination of installed pylon-nacelle drag increments and grid refinement studies. The code-to-code scatter was significantly reduced compared to the first DPW, but still larger than desired. However, grid refinement studies showed no significant improvement in code-to-code scatter with increasing grid refinement. The third Drag Prediction Workshop focused on the determination of installed side-of-body fairing drag increments and grid refinement studies for clean attached flow on wing alone configurations and for separated flow on the DLR-F6 subsonic transport model. This work evaluated the effect of grid refinement on the code-to-code scatter for the clean attached flow test cases and the separated flow test cases.

Nomenclature

AR	= aspect ratio
C_D	= drag coefficient
C_{DP}	= idealized profile drag coefficient, $C_D - C_L^2 / (\pi AR)$
$C_{D_{PR}}$	= pressure drag coefficient
$C_{D_{SF}}$	= skin friction drag coefficient
C_L	= lift coefficient
C_m	= pitching moment coefficient
C_v	= coefficient of variation
K	= coverage factor for individual values
M	= Mach number
n	= number of observations in a sample
Re	= Reynolds number based on mean aerodynamic chord
x_i	= value of an observation
\bar{x}	= sample mean of a set of observations
\tilde{x}	= sample median
μ	= population mean
$\hat{\mu}$	= estimate of the population mean
σ	= population standard deviation
$\hat{\sigma}$	= estimate of the population standard deviation

^{*} Research Scientist, Computational AeroSciences Branch, Mail Stop 128, Senior Member, AIAA.

[†] Aerospace Engineer, Configuration Aerodynamics Branch, Mail Stop 499, Associate Fellow, AIAA.

I. Introduction

IN June 2006, the AIAA Applied Aerodynamics Technical Committee (APATC) sponsored the third Drag Prediction Workshop (DPW-III) for transonic cruise drag predictions of subsonic transports. The workshop was a follow-on to the first Drag Prediction Workshop (DPW-I) held in June 2001^{1,2} and the second Drag Prediction Workshop (DPW-II) held in June 2003^{3,4}. The objectives for these three workshops were (1) to assess the state-of-the-art computational methods as practical aerodynamic tools for aircraft force and moment prediction of industry relevant geometries, (2) to provide an impartial forum for evaluating the effectiveness of existing computer codes and modeling techniques using Navier-Stokes solvers, and (3) to identify areas needing additional research and development.

DPW-I solicited CFD predictions of the lift, drag, and pitching moment for a subsonic transport wing-body configuration. The DLR-F4 wing-body configuration^{5,7} was chosen due to the public availability of the geometry and experimental data from three wind tunnels. The test cases consisted of a single point solution at a fixed value of C_L ($C_L = 0.5 \pm 0.001$), calculation of a drag polar, and an optional calculation of drag rise at a constant value of C_L . DPW-I did not require a grid convergence analysis. A total of 38 solutions were submitted for the workshop from 18 authors using 13 different CFD codes. A summary of the results of the workshop is given in Ref. 1 and a statistical analysis of the results is given in Ref. 2. The code-to-code statistical analysis of the results identified two major surprises²: (1) roughly 20% of the solutions were statistical outliers compared to the others and (2) the code-to-code scatter for drag was more than an order of magnitude larger than desired by airframe designers.

DPW-II focused on the prediction of installed pylon-nacelle drag increments and on grid refinement studies. The DLR-F6⁸ Wing-Body and Wing-Body-Nacelle-Pylon configurations were chosen for DPW-II since DLR and ONERA made data publicly available for this configuration. The test cases consisted of a single point solution at a fixed value of C_L ($C_L = 0.5 \pm 0.001$) for both the DLR-F6 Wing-Body and Wing-Body-Pylon-Nacelle configurations on coarse, medium, and fine grids, and a drag polar. Optional test cases included a comparison of tripped and fully turbulent solutions and calculation of drag rise at a fixed value of C_L . A total of 21 solutions were submitted for the workshop from 20 authors using 18 different CFD codes. There were 16 solutions that calculated all three grid levels for both the DLR-F6 Wing-Body and Wing-Body-Pylon-Nacelle from 15 authors using 15 different CFD codes. A summary of the results is given in Ref. 3 and a statistical analysis of the results is given in Ref. 4. The DLR-F6 configuration had substantial areas of separation at the wing-body juncture and at the wing-pylon juncture. Additionally, there was a region of separation at the trailing edge of the wing. The code-to-code scatter was significantly reduced from DPW-I although it was still an order of magnitude larger than desired by airframe designers. However, there was no significant change in code-to-code scatter with increasing grid density.

The discussion at DPW-II identified three suggestions for DPW-III: (1) the large regions of separation were a likely culprit for the lack of grid convergence and cases should be chosen with minimal separation, (2) simpler cases were required to allow for better grid convergence studies and wider participation, and (3) blind studies were preferable where experimental data were not available *a priori*. It was generally agreed that continuing studies of the DLR-F6 case were warranted. Therefore, Vassberg *et al.*⁹ designed a side-of-body fairing for the DLR-F6, designated the FX2B, to remove the wing-body juncture separation. Additionally, two wings, DPW-W1 and DPW-W2, were designed (see Ref. 10 for a description of this process) for a simple geometry with DPW-W2 a single point optimization of DPW-W1. An experimental program is under development by NASA and DLR to collect data for the DLR-F6 wing-body with and without the FX2B side-of-body fairing. However, no current experimental program is planned to provide data for the DPW-W1 and DPW-W2 wings.

A summary of the results from DPW-III is provided in Ref. 10. Detailed results from participants are provided in Refs. 11-14.

This paper is organized in the following manner. Section II provides a description of the statistical analysis. Section III outlines the test cases for the workshop. Section IV details the statistical results. Section V provides some summary comments.

II. Statistical Approach

Hemsch² introduced the idea of treating different computations of a test case as a collective and using N-version testing in a statistical framework to investigate the submissions. No individual result is considered the “right” or “best” result. The dispersion of the results is treated as noise in the collective computational process.

A running record of individual outcomes is plotted for each of the measures of interest and derived quantities reported by participants. For Case 1, participants reported the angle of attack (α), total drag coefficient (C_D),

pressure drag coefficient ($C_{D_{PR}}$), skin friction drag coefficient ($C_{D_{SF}}$), and moment coefficient (C_m). For Case 2, participants reported the lift coefficient (C_L), total drag coefficient, pressure drag coefficient, skin friction drag coefficient, and moment coefficient. The derived measures of interest for Case 1 and Case 2 were the lift-to-drag ratio (C_L/C_D) and idealized profile drag ($C_{DP} = C_D - C_L^2/\pi AR$). The value of the measure of interest is plotted on the vertical axis and an integer index is used for each data submission on the horizontal index. The order of the solutions on the horizontal axis is irrelevant since this is not a temporal axis, therefore the submissions are grouped according to grid type (multi-block structured, overset structured, unstructured).

An estimate of the population mean $\hat{\mu}$ of the plotted data submissions is made and is shown on the graph as the centerline. Upper and lower scatter limits are placed on the graph as follows:

$$\text{Upper Limit} = \hat{\mu} + K\hat{\sigma} \quad (1)$$

$$\text{Lower Limit} = \hat{\mu} - K\hat{\sigma} \quad (2)$$

where $\hat{\sigma}$ is an estimate of the population standard deviation and K is an appropriate coverage factor. Significant results are outcomes that lie outside the process limits defined in Eqs. (1) and (2). These results, referred to as outliers, represent submissions that are different from the results that lie within the scatter limits (and should be investigated to understand the difference).

The population mean $\hat{\mu}$ is estimated using the sample median, which is given (for sorted data) as:

$$\begin{aligned} \hat{\mu} &= \tilde{x} \\ \tilde{x} &\equiv x_{(n+1)/2} & (n \text{ odd}) \\ \tilde{x} &\equiv 0.5(x_{n/2} + x_{(n/2)+1}) & (n \text{ even}) \end{aligned} \quad (3)$$

The sample median provides a robust estimate when outliers are present. The sample standard deviation

$$\hat{\sigma} = SSD \equiv \sqrt{\frac{1}{n-1} \sum_{i=1}^n (x_i - \bar{x})^2} \quad (4)$$

is used to estimate the population standard deviation. The coverage factor is estimated for a uniform distribution¹⁵ as $K = \sqrt{3}$.

III. Test Cases

Participants were given the option of calculating Case 1, Case 2, or both. All simulations were specified to be in free air, i.e. no wind tunnel walls or model support systems were to be included. The boundary layer was to be modeled as fully turbulent. Grids were made available for the three types (multi-block structured, overset structured, unstructured) or participants could provide their own grids. A summary of the grids and results is provided in Ref. 10. Additional details of individual grid families and results from participants are available in Refs. 11-14.

A. Case 1: DLR-F6 Wing-Body with and without FX2B Fairing

Test Case 1 focused on the DLR-F6 Wing-Body configuration that was the subject of DPW-II. DPW-II matched the experimental Reynolds number of 3 million. DPW-III increased the Reynolds number to 5 million to reduce the region of wing trailing edge separation while remaining within the load limitations of the model. The DLR-F6 Wing-Body had a large separation at the aft wing-body juncture. Vassberg *et al.*⁹ designed a side-of-body fairing, designated FX2B, that eliminated this separation numerically. Participants were required to calculate the total drag coefficient, pressure drag coefficient, skin friction drag coefficient, and pitching moment coefficient for the DLR-F6

Wing-Body with and without the FX2B fairing. Participants were also required to report the separation data and pressure profiles for both configurations and angle of attack for the fixed C_L condition. The Case 1 studies were:

Single Point Grid Convergence Study with Three Grid Levels

Flow conditions:

- Mach = 0.75
- $C_L = 0.5 \pm 0.001$
- $Re = 5$ million

Drag Polar on Medium Grid

Flow conditions:

- Mach = 0.75
- $Re = 5$ million
- $\alpha = \{-3.0, -2.0, -1.0, -0.5, 0.0, 0.5, 1.0, 1.5\}$ degrees

B. Case 2: DPW-W1 and DPW-W2 Wing Alone

Test Case 2 focused on the wing alone configurations. DPW-W2 is a single point optimization of the DPW-W1 wing. Both wings are simple trapezoidal wings with modern supercritical airfoil shapes. Participants were required to calculate the lift coefficient, total drag coefficient, pressure drag coefficient, skin friction drag coefficient, and pitching moment coefficient for both wings. Participants were also required to report the separation data and pressure profiles for both wings. The Case 2 studies were:

Single Point Grid Convergence Study with Four Grid Levels

Flow conditions:

- Mach = 0.76
- $\alpha = 0.5$ degrees
- $Re = 5$ million

Drag Polar on Medium Grid

Flow conditions:

- Mach = 0.76
- $Re = 5$ million
- $\alpha = \{-1.0, 0.0, 0.5, 1.0, 1.5, 2.0, 2.5, 3.0\}$ degrees

IV. Results

A. Case 1: DLR-F6 and FX2B Wing-Body Grid Convergence Study

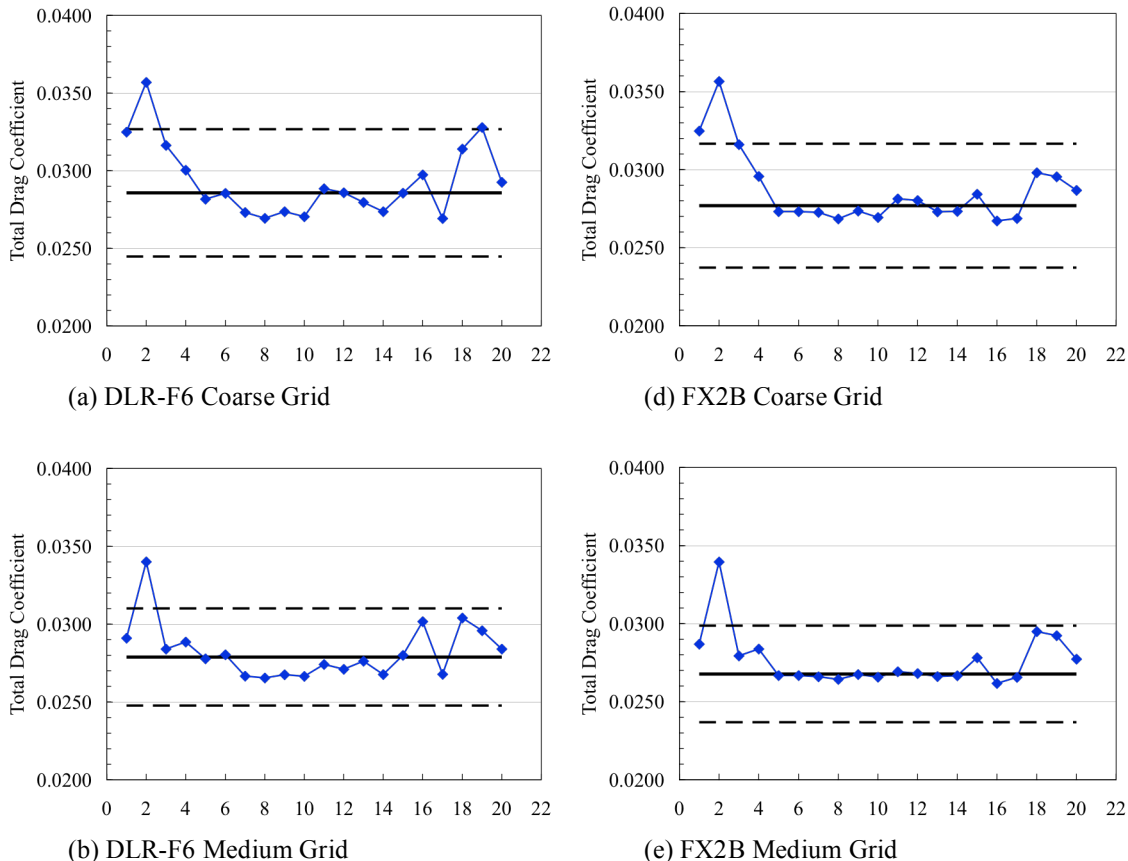
Twenty-six solutions were submitted for Case 1. Not all of these solutions included the coarse, medium, and fine grid levels for both the DLR-F6 and FX2B configurations. The 20 submissions that did include all three grid levels for both configurations are termed the fully nested solutions. The statistical analysis below identifies outliers that are different from the other solutions. The core solutions are the solutions that are similar to each other, i.e. the core solutions are the nested solutions minus the outliers. Table 1 summarizes the data submissions for the DLR-F6 results from DPW-II and Case 1 results from DPW-III. The current results include more submissions but have slightly fewer authors, organizations, and CFD codes. The nested solutions used 9 turbulence models or variants and the core solutions used 8 turbulence models or variants.

Table 1. Comparison of workshop statistics for grid convergence of DLR-F6 wing/body configurations in DPW-II and DPW-III.

	DPW-II			DPW-III		
	Submissions	Nested	Core	Submissions	Nested	Core
Solutions	21	16	13	26	20	16
Authors	20	15	12	15	12	9
Institutions	16	14	11	13	10	9
Codes	18	15	12	14	12	8

1. Individuals Charts for Case 1 Grid Convergence Study

Running records of individual outcomes were plotted for each of the measures of interest, for each grid level in the grid resolution study, and for each configuration for a total of 42 plots for Case 1 (7 measures of interest, 3 grid levels, 2 configurations). Not all of these will be shown here. Figure 1 shows the total drag coefficient for the DLR-F6 and FX2B configurations for the coarse, medium, and fine grid levels. The median, Eq. (3), is shown as the centerline as a solid black line; scatter limits, Eq. (1), are shown as dashed black lines. In all of the following plots for Case 1, the solution index on the abscissa refers to the same solution submission.



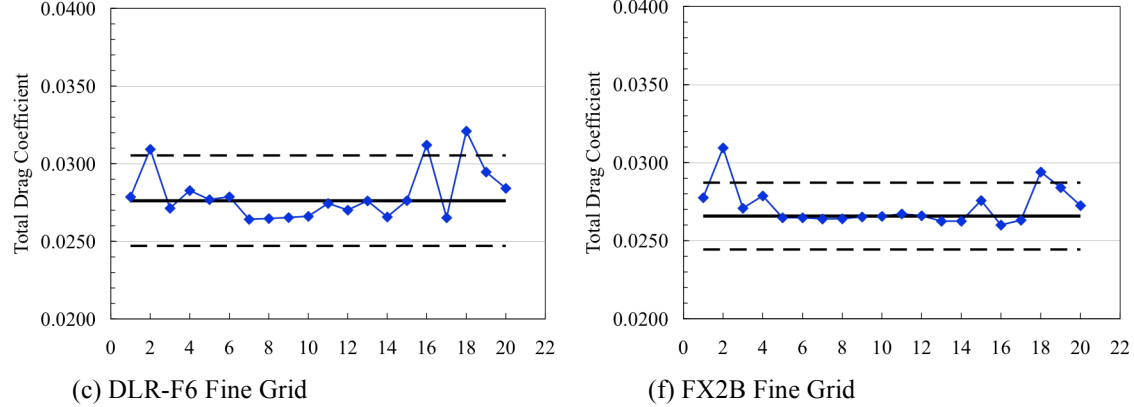


Figure 1. Comparison of individuals charts for the total drag coefficient for the DLR-F6 and FX2B configurations for the cruise point grid convergence study.

Solution 2 is outside the scatter limits for total drag coefficient for all three grid levels and for both the DLR-F6 and FX2B configurations. Three other solutions are outside the scatter limits for one of the configurations on one or more grid levels. Also note that the scatter level decreases as the grid is refined.

Figure 2 shows the fine grid pressure and skin friction drag coefficients for the FX2B configuration. Solution 2 is within the limits for the pressure drag, but the skin friction drag is high and outside the limits for all three grid levels for both the DLR-F6 and FX2B configurations (not all charts shown). (Solution 18 included the total drag coefficient but did not provide the pressure drag coefficient, skin friction drag coefficient, or the pitching moment coefficient. Solution 18 is not plotted and is omitted from the calculation of statistics for those quantities that were not reported.) The scatter levels did not decrease monotonically with grid refinement. This will be shown in the next section.

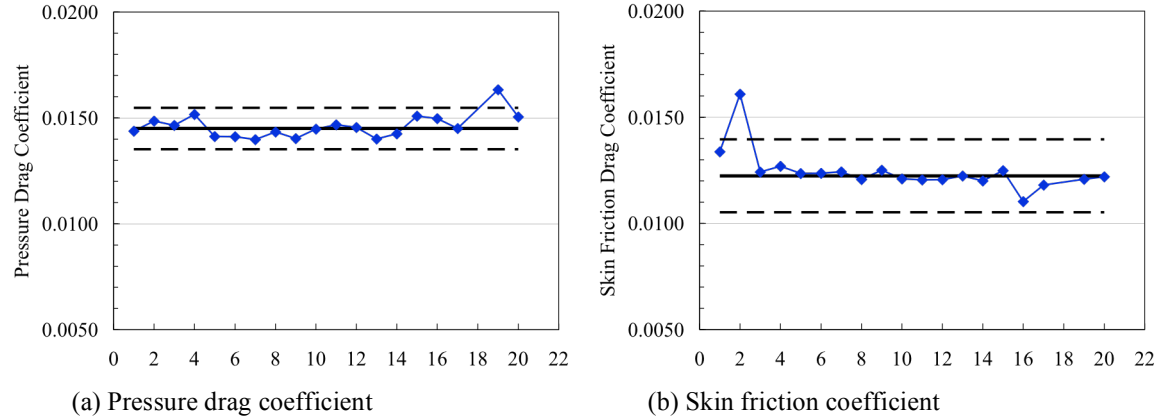


Figure 2. Comparison of individuals charts for the pressure drag coefficient and skin friction drag coefficient for fine grid on the FX2B configuration.

Figure 3 shows the angle of attack and the pitching moment coefficient for the same fine grid solutions for the FX2B configuration. The angle of attack and moment coefficient for Solution 2 are very near the median. This is consistent with the pressure drag prediction. The difference in the total drag coefficient prediction of Solution 2 is clearly due to the skin friction.

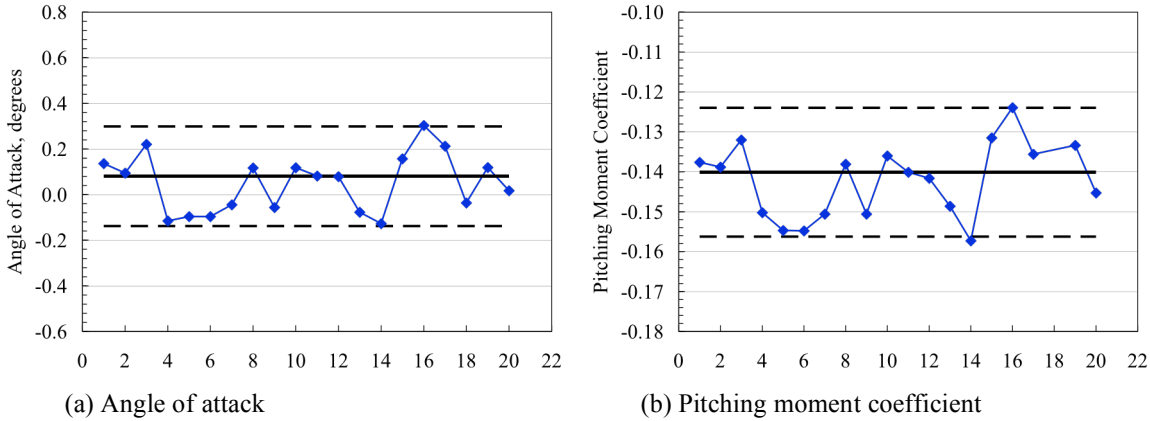


Figure 3. Individuals charts for angle of attack and pitching moment coefficient for the fine grid on the FX2B configuration.

Solution 2 used the same grid, the same CFD code, and was provided by the same authors as Solutions 1 and 3. The difference between Solutions 1, 2, and 3 is solely the turbulence model. Solutions 1 and 3 used algebraic stress turbulence models; Solution 2 used a linear k - ϵ turbulence model. The k - ϵ turbulence model reported in Solution 2 predicts a different skin friction level than the other solutions.

2. Grid Convergence Results

It is difficult to see grid related trends in the data from the individuals charts. Therefore, all three grid levels were plotted together for each measure of interest for the DLR-F6 and FX2B configurations. The median and scatter limits were included with the plots of variation.

In order to compare results on unstructured meshes with results on multi-block structured meshes and overset structured meshes, it is convenient to use a one-dimensional estimate of the grid spacing

$$h = \frac{1}{\sqrt[3]{NPTS}}$$

where NPTS is the number of solution points (for either cell-centered or vertex based CFD codes) in the mesh. Second order accurate results will lie on a straight line when plotted versus h^2 ($NPTS^{-2/3}$). An additional benefit of plotting versus $NPTS^{-2/3}$ is that coarse meshes show up on the right of the plot and finer grids approach the y-axis, which is the limit of infinite grid resolution.

Salas^{16,17} has shown that the error is linear with h^p (where p is the order of accuracy of the scheme) only if the grid is refined uniformly in all coordinate directions, e.g. if the grid spacing is halved in the x coordinate, it must also be halved in the y and z coordinates. The gridding guidelines posted to guide development of grids for the workshop (http://aaac.larc.nasa.gov/tsab/cfdlarc/aiaa-dpw/Workshop3/gridding_guidelines.html), included this as a requirement for structured grids for the Case 2 Wing Alone grid convergence studies and as a recommendation for structured grids for Case 1 DLR-F6 and FX2B due to the greater difficulty in generating these grids. The gridding guidelines required that the grid convergence cases maintain the same family of grids between grid levels. It was noted at the workshop that not all of the grids submitted for the workshop met these requirement. Therefore, plots for these grids will not necessarily achieve second order accuracy and will not show up as a straight line on these plots. Other factors can also contribute to this non-linearity.

Figure 4 shows the variation of the total drag coefficient for the nested solutions of both the DLR-F6 and FX2B configurations. In the following variation plots, the median is shown as solid black squares connected with a solid black line, the scatter limits are shown as dashed black lines, multi-block structured grids are plotted with blue symbols and lines, overset structured meshes are plotted with red symbols and lines, and unstructured meshes are

plotted with green symbols and lines. Solution 2 (solid blue diamonds) is clearly outside the scatter limits confirming what was shown in Fig. 1. The reason for the difference in Solution 2 is attributed to its use of a linear $k-\epsilon$ model. The DLR-F6 total drag coefficient for Solutions 16 (green triangle) and 18 (green asterisk) increases as the grid is refined, falling outside the scatter limits for the finest grid, while the other solutions decrease or remain constant.

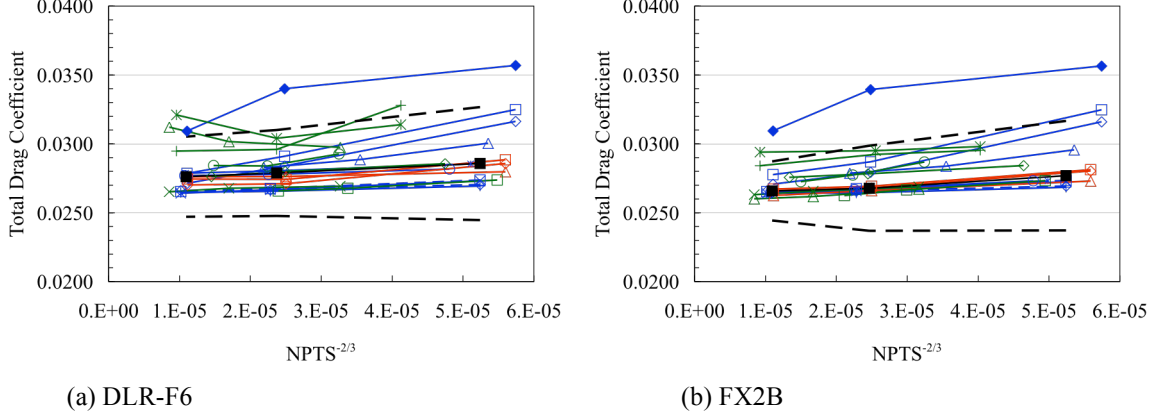


Figure 4. Grid convergence of total drag coefficient including median and scatter limits.

Figure 5 shows the variation of the pressure drag coefficient for the DLR-F6 and FX2B configurations. Solution 16 is outside the scatter limits for the DLR-F6 and increases with mesh refinement. The pressure drag coefficient for Solution 16 is high but the skin friction drag is lower than the median resulting in the total drag coefficient falling within the scatter limits for all cases except the DLR-F6 fine grid. Solution 18, which showed a similar trend to Solution 16 for the total drag coefficient in Fig. 4, is not plotted as the drag component data were not provided. Solution 19 (green plus sign) distinctly falls outside the scatter limits for the pressure drag coefficient on the coarse mesh for DLR-F6 and all three mesh levels for FX2B. The scatter for the pressure drag coefficient decreases with grid refinement for the FX2B but not for the DLR-F6.

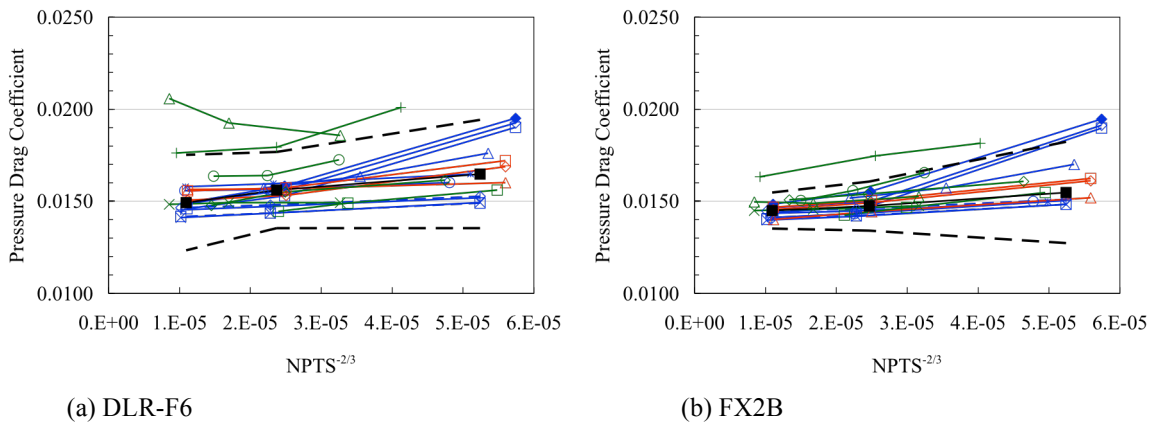


Figure 5. Grid convergence of pressure drag coefficient including mean and scatter limits.

Figure 6 shows the variation of the skin friction drag coefficient for all three grid levels of the DLR-F6 and FX2B. The skin friction drag coefficient for Solution 2 is high and well outside the scatter limits for all grid levels and both configurations. There is very little variation with grid level for most of the solutions for skin friction. The skin friction drag coefficient levels and grid variation is almost identical for the DLR-F6 and FX2B configurations.

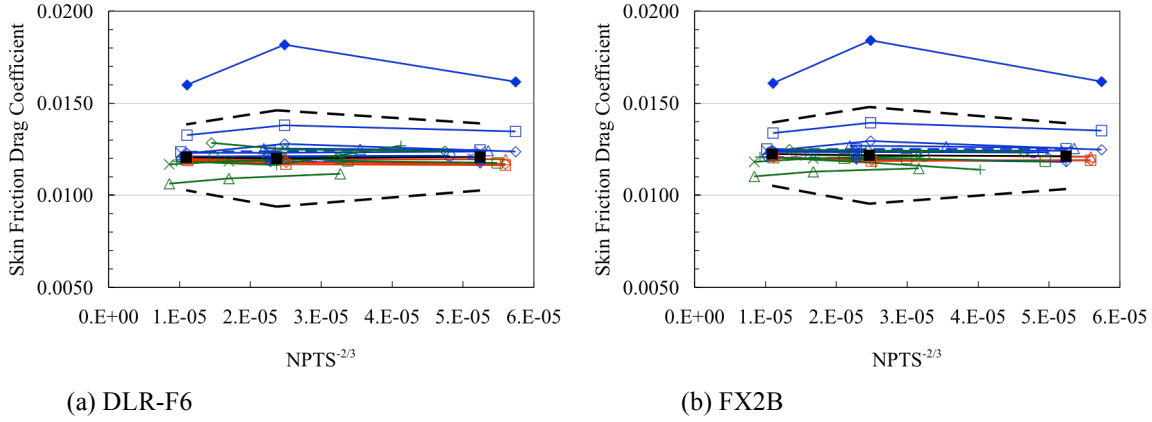


Figure 6. Grid convergence of skin friction drag coefficient including mean and scatter limits.

The variation of angle of attack for the DLR-F6, Fig. 7(a), is substantially larger than the variation for the FX2B, Fig. 7(b). The angle of attack for Solution 16 increases substantially with grid resolution for the DLR-F6. The angle of attack for Solution 18 decreases substantially for the finest grid on the DLR-F6.

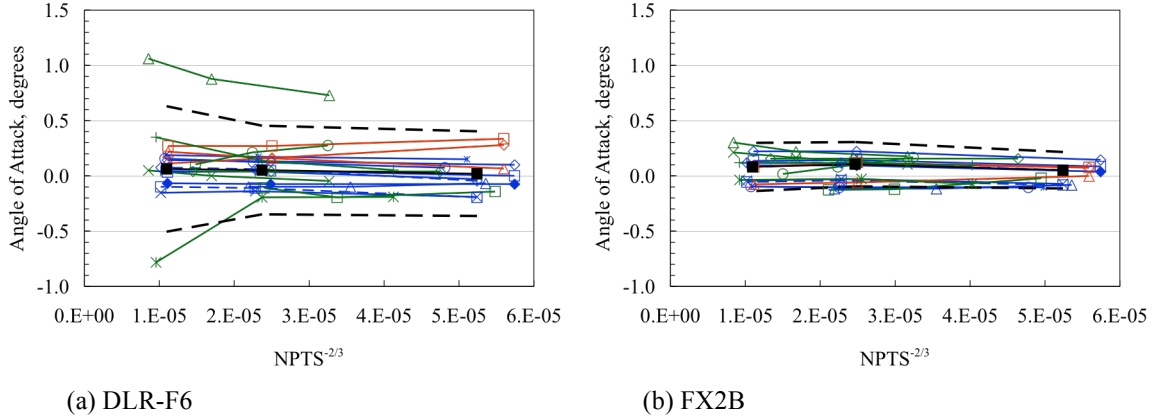


Figure 7. Grid convergence of angle of attack including mean and scatter limits.

Figure 8 shows the variation in the pitching moment coefficient for all three grid levels for both the DLR-F6 and FX2B. The pitching moment for Solution 16 increases with grid refinement for the DLR-F6 which is consistent with the increase in angle of attack seen in Fig. 7(a). Pitching moment data were not submitted for Solution 18.

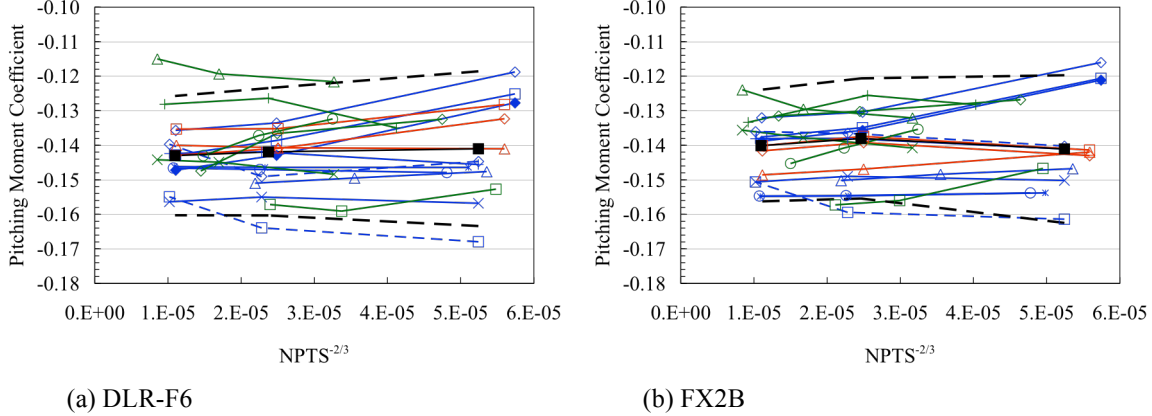


Figure 8. Grid convergence of pitching moment coefficient including mean and scatter limits.

The individuals charts in Fig. 1 and grid convergence charts in Figs. 4 and 6 shows that the total drag coefficient and pressure drag coefficient for Solution 2 is consistently high and outside the scatter limits. Fig. 5(a) shows that the pressure drag coefficient for Solution 16 is high and outside the scatter limits and increases for the DLR-F6 configuration with increasing grid resolution. Fig. 5 shows that pressure drag coefficient is high for Solution 19 and outside the limits for the coarse grid on DLR-F6 and all grid levels for FX2B. Fig. 7 shows that Solutions 16 and 18 have different trends for angle of attack from the other solutions and are outside the scatter limits. Solution 18 showed a similar trend to Solution 16 for the total drag coefficient but drag components were not provided to see pressure and skin friction drag coefficients. The outliers were determined from this analysis to be these four solutions: 2, 16, 18, and 19.

It was previously shown that Solution 2 differs from the other solutions because of the turbulence model. It is not as clear why Solutions 16, 18, and 19 differ from the core solutions. Solutions 16, 18, and 19 all used the Spalart-Allmaras (SA) turbulence model¹⁸, but so did Solutions 7, 9, 13, 14, 17, and 20 all of which are in the core. Solution 16 used the LaRC generated unstructured grid, but so did Solution 17 which is in the core. Solution 16 used an all tetrahedral mesh while Solution 17, which was in the core, used a hybrid mesh with the same grid points, but Solutions 18 and 19 used hybrid meshes and were outliers. Solutions 18 and 19 both used the same grids that were different from Solution 16 and Solution 18 had similar behavior for total drag coefficient as Solution 16. Solution 16 used full Navier-Stokes rather than the thin-layer assumption, but Solutions 9 and 10 also used full Navier-Stokes and were in the core. Furthermore, Solution 7 used the thin-layer assumption and Solution 9 used full Navier-Stokes with everything else the same and both were in the core. Solutions 8 and 10 also only differed in the thin-layer/full Navier-Stokes assumption and both were in the core. There does not appear to be a single main effect among the characteristics that were gathered that explain why these solutions differ from the other solutions. It is important to continue to investigate the cause of these differences in detail to identify improvements to CFD codes and solution processes.

3. Core Solutions

The core solutions are the 20 fully nested solutions minus the four outliers determined in the previous section (Solutions 2, 16, 18, and 19). The median values for the Case 1 core solutions at all three grid levels is given in Table 2. Table 3 shows the standard deviations for the core solutions of Case 1. The variation of the core solutions is shown in Figures 9-13 including new estimates of the median and scatter limits for the core solutions. The variation of the core solutions is substantially reduced from the nested solutions. The variation of the core solutions for the total drag and pressure drag coefficients decreases with grid refinement and is more monotonic than the nested solutions. From Table 3, it is seen that the standard deviation for the total drag is approaching 5-7 drag counts for the fine grid core solutions.

Table 2. Comparison of Case 1 core medians.

	DLR-F6			FX2B		
	Coarse	Medium	Fine	Coarse	Medium	Fine
α , degrees	0.0200	0.0535	0.0625	0.0515	0.0985	0.0480
C_D , counts	284	275	273	273	267	265
$C_{D_{PR}}$, counts	161	154	149	153	146	144
$C_{D_{SF}}$, counts	120	120	121	122	123	123
C_m	-0.145	-0.143	-0.144	-0.142	-0.140	-0.143

Table 3. Comparison of Case 1 core standard deviations.

	DLR-F6			FX2B		
	Coarse	Medium	Fine	Coarse	Medium	Fine
α , degrees	0.16	0.13	0.12	0.096	0.12	0.12
C_D , counts	16	8.4	6.8	17	7.3	5.5
$C_{D_{PR}}$, counts	14	6.3	6.5	14	4.8	3.9
$C_{D_{SF}}$, counts	4.6	5.3	4.0	4.2	5.2	3.6
C_m	0.0128	0.0087	0.0067	0.0120	0.0094	0.0085

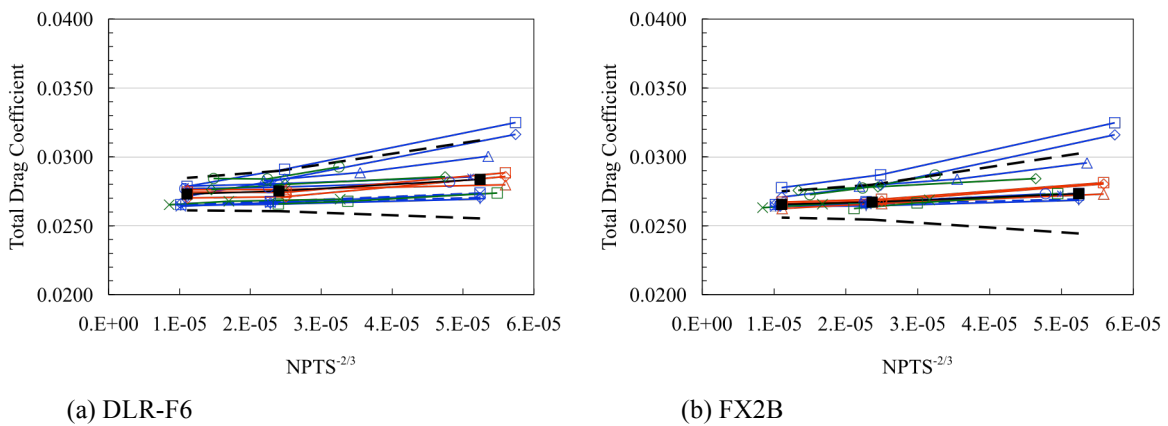


Figure 9. Comparison of total drag coefficient for core solutions including median and scatter limits.

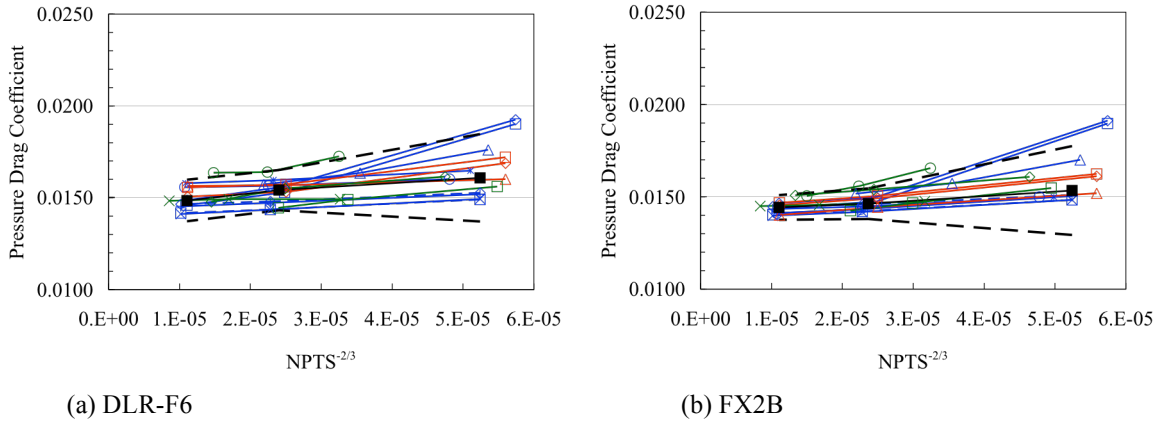


Figure 10. Comparison of pressure drag coefficient for core solutions including median and scatter limits.

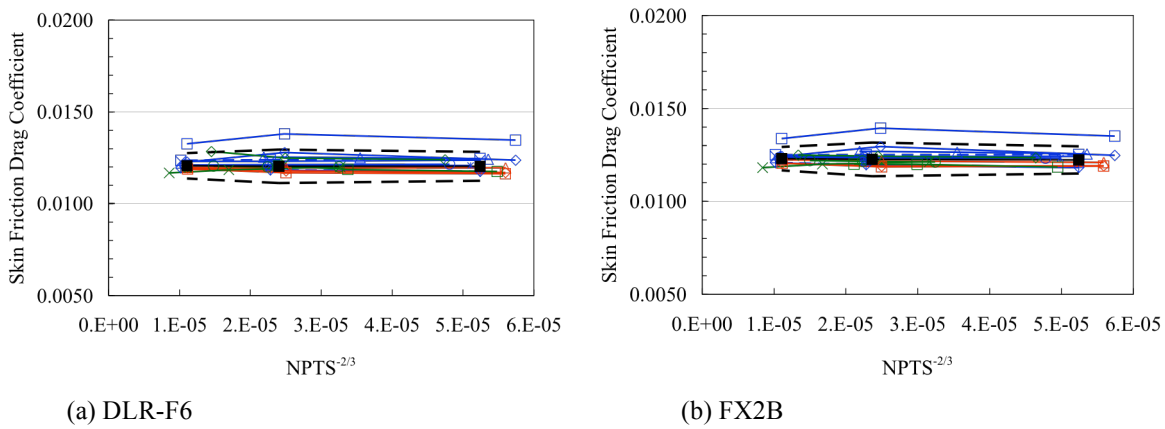


Figure 11. Comparison of skin friction drag coefficient for core solutions including mean and scatter limits.

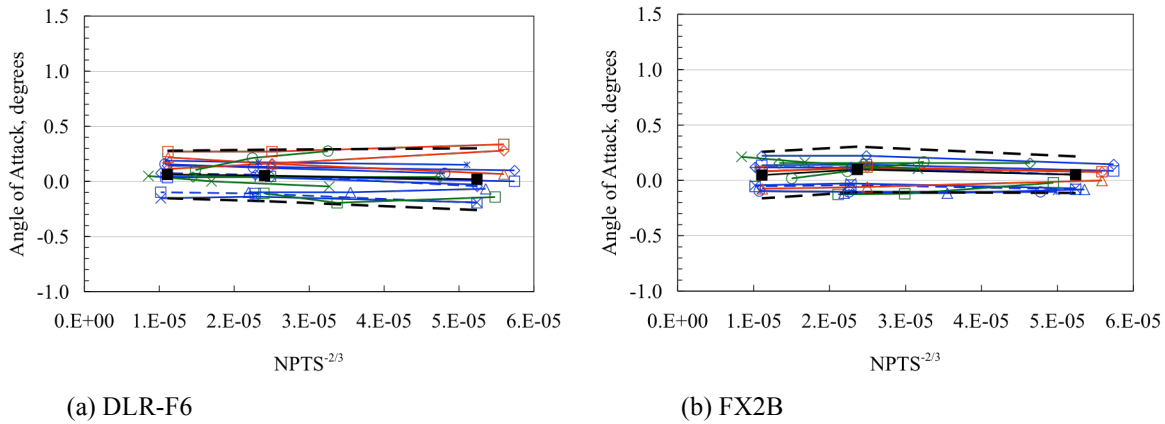
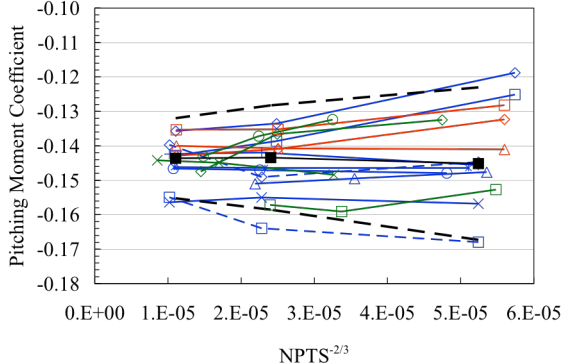
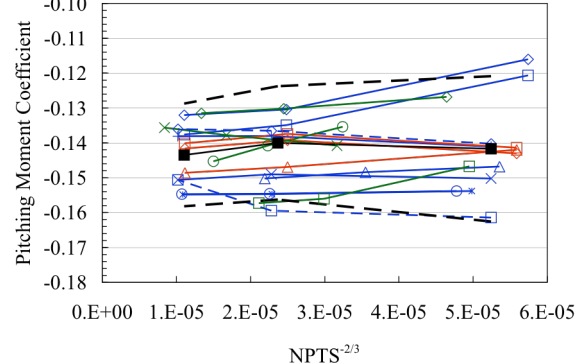


Figure 12. Comparison of angle of attack for core solutions including mean and scatter limits.



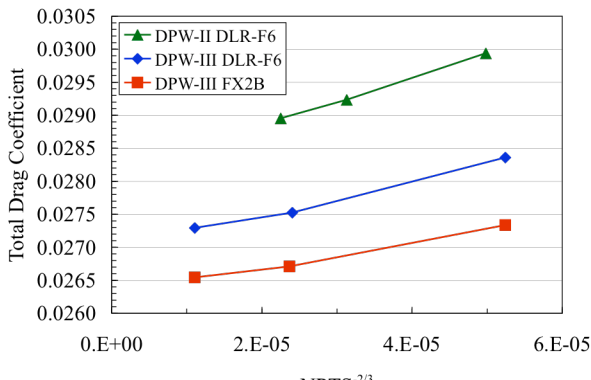
(a) DLR-F6



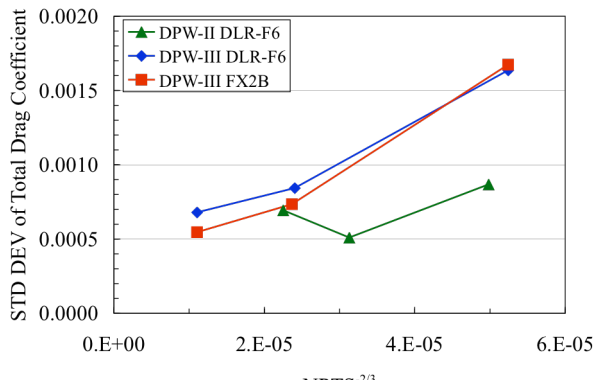
(b) FX2B

Figure 13. Comparison of pitching moment coefficient for core solutions including median and scatter limits.

Figure 14 shows the grid convergence of the median and standard deviation of the total drag coefficient for the core solutions for the DLR-F6 (blue diamonds and line) and the FX2B (red squares and line). The DPW-II wing-body results from DPW-II (green triangle and line) at a lower Reynolds number ($Re = 3$ million) are included for comparison. The drag for the DPW-II DLR-F6 at the lower Reynolds number is higher than the drag for the DLR-F6 from DPW-II at $Re=5$ million. The drag on the FX2B configuration is lower still as the FX2B has attached flow without separation at the wing-body juncture. It is also clear that the grid sizes increased from DPW-II to DPW-III. However, the standard deviation of the total drag coefficient is lower for the DPW-II results on the coarser grid than the DPW-III results. The standard deviation is lower for DPW-III only for the FX2B configuration on the finest grid. The standard deviations decrease monotonically for the Case 1 DLR-F6 and FX2B configurations while the DPW-II results were not monotonic. The lack of monotonicity in the DPW-II results may be from grids that were not consistently refined. However, since all three of these results have different means, the standard deviations cannot be directly compared. Section IV.C has further analysis of the variation of these data along with Case 2.



(a) Median



(b) Standard deviation

Figure 14. Grid convergence of total drag coefficient median and standard deviation of the core solutions.

B. Case 2: DPW-W1 and DPW-W2 Wing Alone Grid Convergence Study

Twelve solutions were submitted for Case 2. Ten of these solutions were nested, i.e. included all four grid levels for both the DPW-W1 and DPW-W2 wing configurations. Table 4 summarizes the data submissions for Case 2. There were about half as many submissions for Case 2 as there were for Case 1. The nested solutions used 5 turbulence models or variants.

Table 4. Comparison of workshop statistics for grid convergence of Case 2 wing alone configurations.

	DPW-W1 and DPW-W2 Wings	
	Submissions	Nested
Solutions	12	10
Authors	10	8
Institutions	8	7
Codes	8	7
Turbulence models and variants	6	5

Running records of individual outcomes were plotted for each of the measures of interest, for each grid level in the grid resolution study, and for each configuration for a total of 56 plots for Case 2 (7 measures of interest, 4 grid levels, 2 configurations). (Note that the index of solution is renumbered from Case 1.) All of these individuals charts (not shown) were reviewed and no solutions were identified as clear outliers. Figures 15-19 show the code-to-code scatter for the lift coefficient, the total drag coefficient, the pressure drag coefficient, the skin friction drag coefficient, and the pitching moment coefficient. None of the solutions fall clearly outside of the scatter limits in a consistent pattern. Therefore, all of the nested solutions are determined to be in the core solutions. The scatter increases for all of these measures as the grid is refined. This is a surprising result since this is the simpler configuration. The scatter for Case 1 decreased with increasing grid refinement.

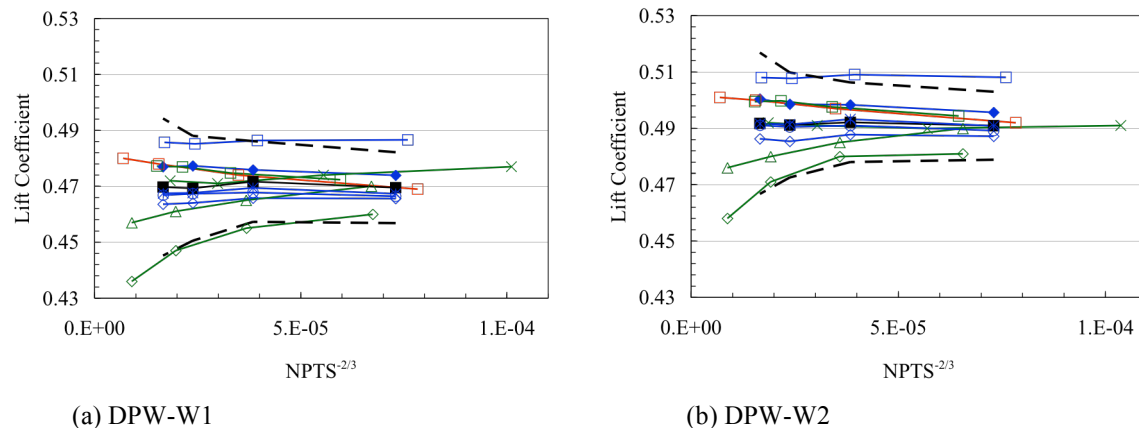
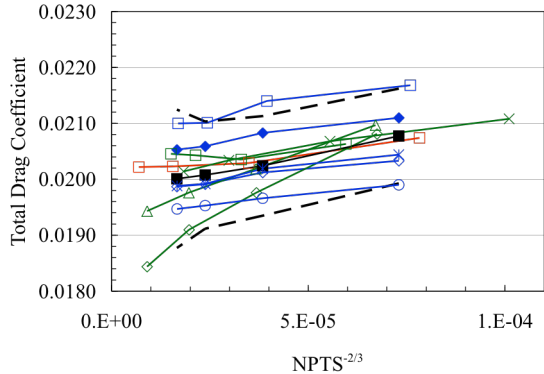
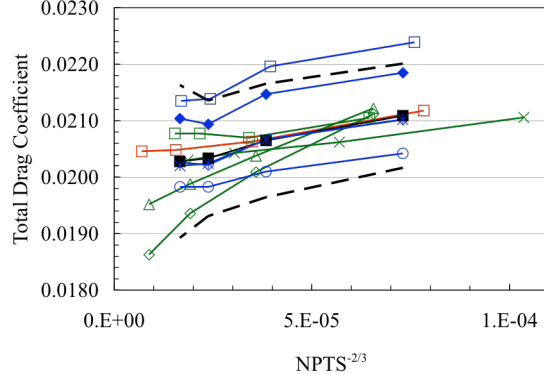


Figure 15. Comparison of coefficient of lift for DPW-W1 and DPW-W2.

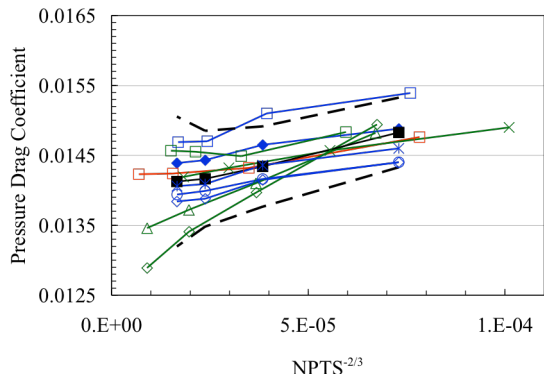


(a) DPW-W1

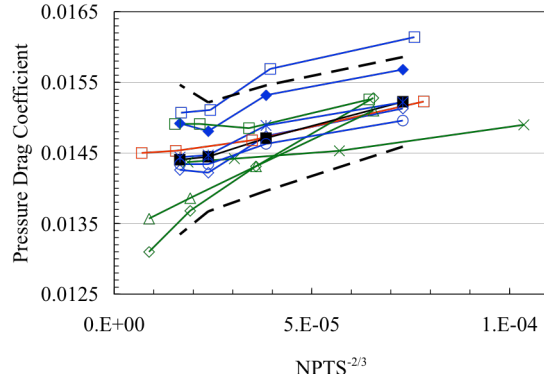


(b) DPW-W2

Figure 16. Comparison of total drag coefficient for DPW-W1 and DPW-W2.

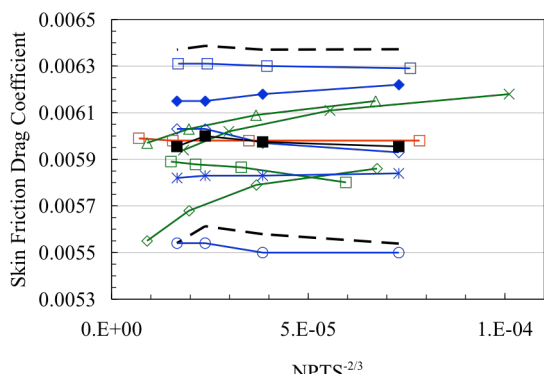


(a) DPW-W1

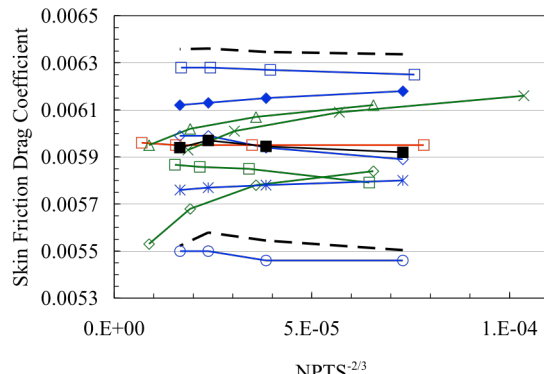


(b) DPW-W2

Figure 17. Comparison of pressure drag coefficient for DPW-W1 and DPW-W2.



(a) DPW-W1



(b) DPW-W2

Figure 18. Comparison of skin friction drag coefficient for DPW-W1 and DPW-W2.

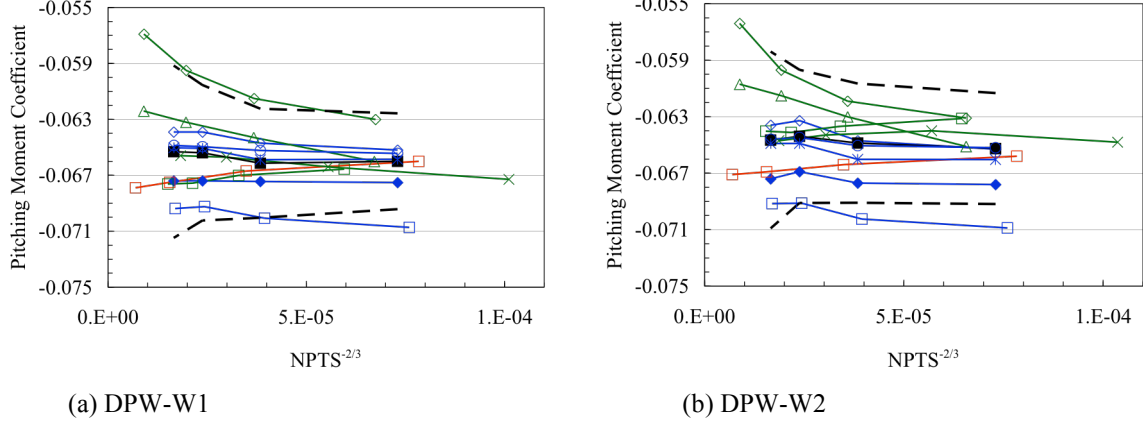


Figure 19. Comparison of pitching moment coefficient for DPW-W1 and DPW-W2.

Case 2 was specified as a constant angle of attack case. The lift was a calculated value and varied as would be expected with solution and grid level. Fig. 15 shows the median and variation of the lift coefficient. The variation of the lift coefficient increases with increasing grid refinement. The drag has a component that is due to the lift. Therefore, a portion of the drag variation is due to the lift variation. Two derived quantities, the lift-to-drag ratio and the idealized profile drag coefficient, account in part for this variation of the lift in the drag. Figure 20 shows the variation in the lift-to-drag ratio for both the DPW-W1 and DPW-W2 wings. The median and scatter limits are also shown. The lift-to-drag ratio is higher for the DPW-W2 configuration, which was the one point optimization of DPW-W1. The variation is almost constant with grid refinement for both configurations, contrary to the variation seen in the lift and total drag.

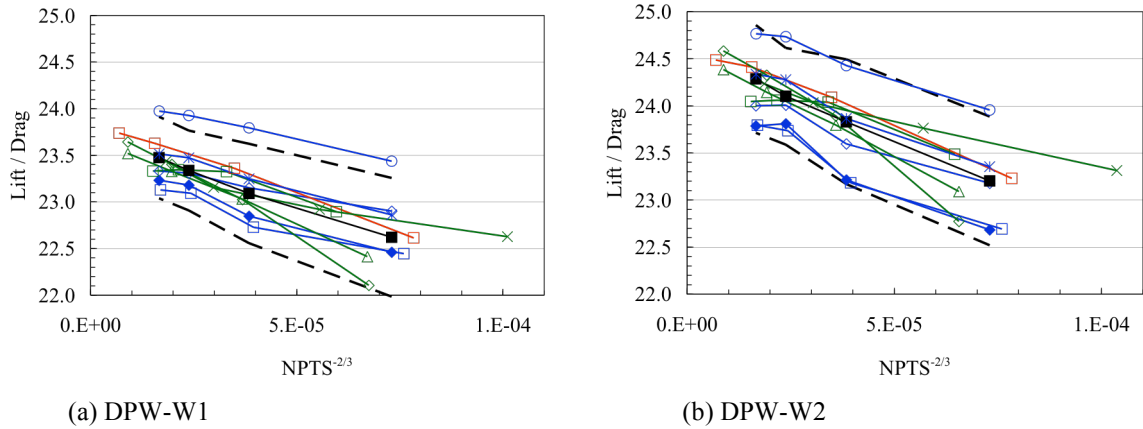


Figure 20. Comparison of lift-to-drag ratio for DPW-W1 and DPW-W2.

Figure 21 shows the variation in the idealized profile drag coefficient for both wing configurations. The idealized profile drag coefficient is lower for the optimized DPW-W2 configuration. The variation is again almost constant with grid refinement. Assessing the variation without accounting for the lift component of drag leads to a different result that the variation increases with grid refinement.

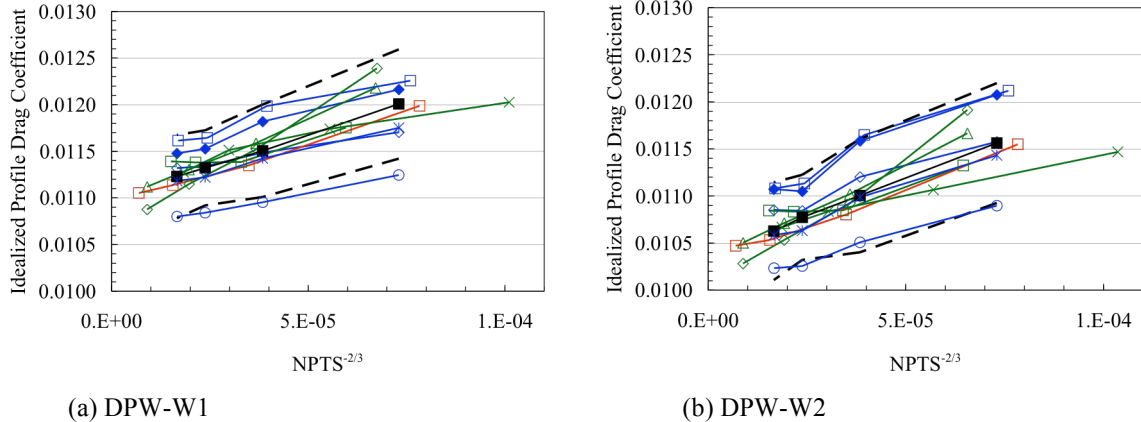


Figure 21. Comparison of idealized profile drag coefficient for DPW-W1 and DPW-W2.

The median values for the Case 2 nested/core solutions at all four grid levels is given in Table 5. Table 6 gives the standard deviations for the nested/core solutions of Case 2. It is interesting to note that even though the standard deviation for the total drag coefficient behaves contrary to expectations by increasing with grid refinement, its level is less than 8 drag counts for all grid levels. This is very similar in magnitude to the standard deviation levels seen for the Case 1 wing-body configurations on the medium and fine grids.

Table 5. Comparison of Case 2 core medians.

	DPW-W1				DPW-W2			
	Coarse	Medium	Fine	Extra Fine	Coarse	Medium	Fine	Extra Fine
C_L	0.470	0.472	0.469	0.470	0.491	0.492	0.491	0.492
C_D , counts	208	202	201	200	211	207	203	203
$C_{D_{PR}}$, counts	148	143	142	141	152	147	144	144
$C_{D_{SF}}$, counts	60	60	60	60	59	59	60	59
C_m	-0.0660	-0.0661	-0.0654	-0.0653	-0.0653	-0.0649	-0.0644	-0.0647

Table 6. Comparison of Case 2 core standard deviations.

	DPW-W1				DPW-W2			
	Coarse	Medium	Fine	Extra Fine	Coarse	Medium	Fine	Extra Fine
C_L	0.0073	0.0083	0.0108	0.0142	0.0070	0.0082	0.0108	0.0145
C_D , counts	4.9	5.1	5.5	7.1	5.3	5.8	5.9	7.8
$C_{D_{PR}}$, counts	2.9	3.3	4.0	5.4	3.7	4.3	4.5	6.1
$C_{D_{SF}}$, counts	2.4	2.3	2.2	2.4	2.4	2.3	2.3	2.4
C_m	0.0020	0.0023	0.0028	0.0036	0.0023	0.0024	0.0027	0.0036

C. Comparison of DPW-II and DPW-III

The coefficient of variation¹⁹, C_v ($= \sigma/\mu$), provides a measure to compare the variation of populations with different means. Figure 22 compares the coefficient of variation of the total drag coefficient and the pitching moment coefficient for the five configurations considered, DPW-II DLR-F6, DPW-III DLR-F6, DPW-III FX2B, DPW-W1,

and DPW-W2, across all grid levels (3 grid levels for DLR-F6 and FX2B; 4 grid levels for DPW-W1 and DPW-W2). The DPW-II DLR-F6 results are at $Re = 3$ million and the DPW-III DLR-F6 results are at $Re = 5$ million. The coefficient of variation for the total drag coefficient and pitching moment coefficient show similar trends:

- the variation for the DPW-III DLR-F6 and FX2B are very similar
- the variation of the DPW-W1 and the DPW-W2 are very similar
- the DPW-II DLR-F6 variation levels for total drag are lower than the DPW-III DLR-F6 and FX2B variation levels
- the DPW-II DLR-F6 variation levels are very near the levels of the DPW-W1 and DPW-W2
- the variation of the DPW-III DLR-F6 and FX2B is decreasing monotonically with increasing grid refinement
- the variation of the DPW-W1 and DPW-W2 wings is increasing with grid refinement
- the variation of DPW-II DLR-F6 is non-monotonic.

The standard deviation of total drag coefficient for the DPW-III DLR-F6 and FX2B configurations decreases from about 6% of the mean total drag coefficient on the coarse grid to about 2% on the fine grid. However, the standard deviation of the total drag coefficient for the DPW-W1 and DPW-W2 wing configurations increases from about 2% of the mean total drag coefficient on the coarse grid to about 4% of mean for the fine grid.

The standard deviation of the pitching moment coefficient for the DPW-III DLR-F6 and FX2B configurations decreases from about 9% of the mean pitching moment for the coarse grid to about 4.5-6% of the mean for the fine grid, with the DLR-F6 having the lower value of variation. The standard deviation for the pitching moment coefficient of the DPW-W1 and DPW-W2 wing configurations increases from about 3-3.5% of the mean pitching moment on the coarse grid to about 5.5% of the mean value on the fine grid.

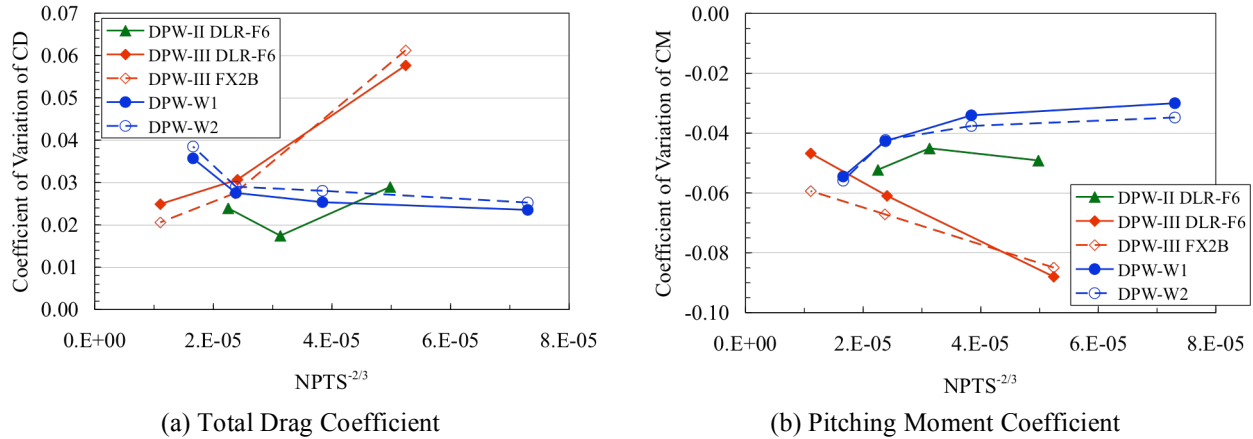
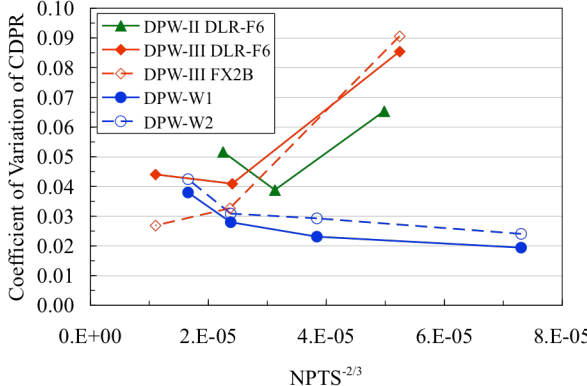
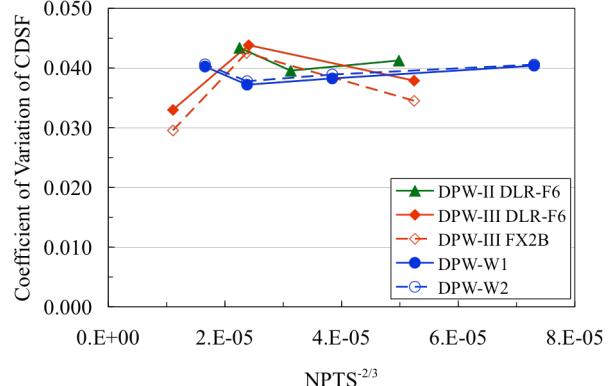


Figure 22. Comparison of coefficient of variation for total drag coefficient and pitching moment coefficient.

The coefficient of variation for the pressure and skin friction drag coefficients is shown in Figure 23. The trends for the pressure drag coefficient nearly mirror the total drag coefficient except (1) the variation of the pressure drag coefficient for the DPW-III DLR-F6 is noticeably larger than the FX2B for the fine grid (about 2.5% versus about 4.5%) and (2) the variation of the pressure drag for the DPW-II DLR-F6 is closer to the variation for the DPW-III DLR-F6 than the total drag variation is. There is minimal variation in the skin friction drag for the DPW-W1 and DPW-W2 wing configurations except at the finest grid. The variation in the skin friction for the DPW-II DLR-F6, the DPW-III DLR-F6, and the FX2B configurations are almost indistinguishable and non-monotonic.



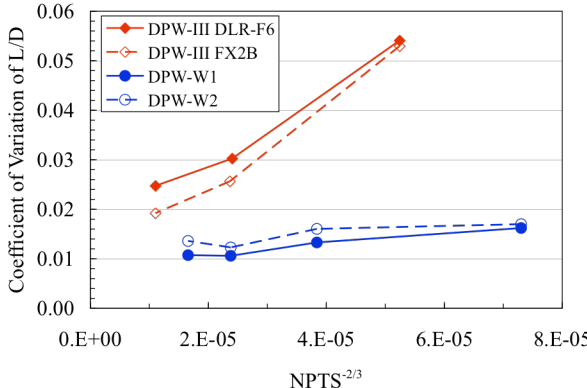
(a) Pressure Drag Coefficient



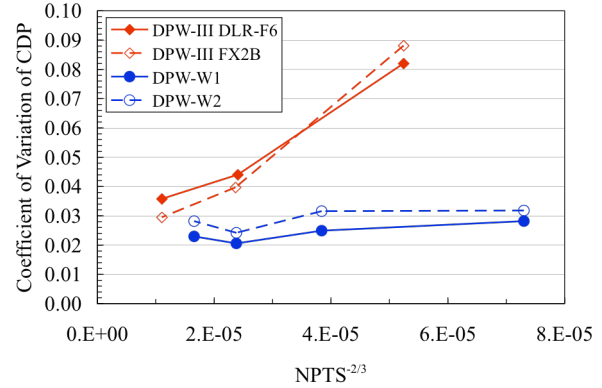
(b) Skin Friction Drag Coefficient

Figure 23. Comparison of coefficient of variation for pressure drag coefficient and skin friction drag coefficient.

Case 1 was a constant lift case and Case 2 was a constant angle of attack case. As discussed earlier, the lift varied for Case 2 and the drag has a component due to lift. Comparing the drag when the lift varies resulted in larger scatter for Case 2 than was seen when the drag component due to lift was corrected. The two derived quantities, lift-to-drag ratio and idealized profile drag, give a better estimate of the variation at the same level of lift. Figure 24 shows the variation for the DPW-III DLR-F6, FX2B, DPW-W1, and DPW-W2 configurations. The variation for the DLR-F6 and FX2B look very similar to the total drag variation, but now the variation for the DPW-W1 and DPW-W2 is substantially smaller (approximately 1% of mean for lift-to-drag ratio and approximately 2-3% of mean for idealized profile drag) than the total drag coefficient. More interestingly, the variation for the DPW-W1 and DPW-W2 has very little change with grid refinement. The variation of DLR-F6 and FX2B still has a large decrease with increasing grid refinement.



(a) Lift-to-Drag Ratio



(b) Idealized Profile Drag Coefficient

Figure 24. Comparison of coefficient of variation for lift-to-drag ratio and idealized profile drag.

The coefficient of variation for the lift-to-drag ratio and the idealized profile drag is substantially lower across all grid levels for the DPW-W1 and DPW-W2 wing configurations than the DLR-F6 and FX2B wing-body configurations. There is a minor reduction in variation for the FX2B configuration compared to the DLR-F6 which may not be statistically significant. The C_v plots for the pressure drag coefficient showed a similar decrease in

variation for the FX2B from the DLR-F6 but the pitching moment coefficient showed a decrease in variation for the DLR-F6 compared to the FX2B.

Variation in the solutions is due to several factors including numerical error, differences in modeling (e.g. turbulence models), user effects (e.g. different levels of iterative convergence), and differences in CFD codes. Well constructed grid convergence studies provide a method to estimate the numerical error and to reduce the numerical error to any required level (limited only by resources and round-off error). DPW-III included grid convergence studies to address numerical errors. However, different models (8 different turbulence models were submitted for Case 1), user processes, and codes were represented. Unfortunately, not all possible combinations of these factors are included, limiting the ability to calculate main effects and higher-order interactions between effects. Case 2 showed a nearly constant coefficient of variation independent of grid refinement. Case 1 approached this value with grid refinement. Further studies would be required to determine if the level of variation achieved in Case 2 and approached on the finest grid level in Case 1 is the inherent variation due to these other factors and the numerical error is negligible.

V. Concluding Remarks

The third Drag Prediction Workshop focused on blind tests of a wing-body configuration and a wing alone configuration. There were no experimental data for any of these cases that could be used to guide the solution process. The DLR-F6 and FX2B configurations for Case 1 demonstrated a monotonic decrease in variation with increasing grid resolution; this is an improvement from DPW-II. However, the level of variation at the coarse and medium grid levels for DPW-II was lower for the total drag and pressure drag than the wing-body variation for DPW-III. The DPW-W1 and DPW-W2 demonstrated a nearly grid independent variation for total drag when the lift component was appropriately accounted for. The variation for the wing alone cases was significantly smaller for the coarser grids than the wing-body cases, but the variation for the wing-body cases approached the value of the variation for the wing alone cases at the highest grid resolution.

The variation for the core solutions of the DLR-F6 configuration, which included separation at the wing-body juncture, was approximately the same as the variation of the FX2B configuration, which had no separation at the wing-body juncture.

After three workshops, it is still clear that grids remain a first order effect and obtaining high quality grids is the first step to obtaining a high quality solution. Furthermore, obtaining a high quality family of grids for relatively simple wing-body configurations suitable for grid convergence studies remains a formidable challenge. Software tools to develop a family of grids rather than a single grid would provide an immense improvement in the CFD process.

The cause of the differences in the solutions was explored. The reason for one structured grid solution differing from the others was ascertained to be the use of a linear $k-\epsilon$ turbulence model. The cause of differences for three unstructured solutions is still unknown. It is imperative to investigate these outliers to identify why they are different in order to improve all CFD codes and processes.

Acknowledgments

The authors thank Dr. C. L. Rumsey and Dr. J. M. Luckring of the NASA Langley Research Center and Dr. J. C. Vassberg of The Boeing Company for their constructive comments, the AIAA Applied Aerodynamics Technical Committee for sponsoring the Drag Prediction Workshops, and the DPW-III Organizing Committee. The authors especially thank the participants of DPW-III.

References

- ¹Levy, D. W., Zickuhr, T., Vassberg, J., Agrawal, S., Wahls, R. A., Pirzadeh, S., and Hemsch, M. J., "Data Summary from the First AIAA Computational Fluid Dynamics Drag Prediction Workshop," *Journal of Aircraft*, Vol. 40, No. 5, 2003, pp. 875-882.
- ²Hemsch, M. J., "Statistical Analysis of Computational Fluid Dynamics Solutions from the Drag Prediction Workshop," *Journal of Aircraft*, Vol. 41, No. 1, 2004, pp. 95-103.
- ³Laflin, K. R., Klausmeyer, S. M., Zickuhr, T., Vassberg, J. C., Wahls, R. A., Morrison, J. H., Brodersen, O. P., Rakowitz, M. E., Tinoco, E. N., and Godard, J-L., "Data Summary from Second AIAA Computational Fluid Dynamics Drag Prediction Workshop," *Journal of Aircraft*, Vol. 42, No. 5, 2005, pp. 1165-1178.
- ⁴Hemsch, M. J., and Morrison, J. H., "Statistical Analysis of CFD Solutions from 2nd Drag Prediction Workshop," AIAA-2004-0556, January 2004.

⁵Redeker, G., "DLR-F4 Wing Body Configuration," in *A Selection of Experimental Test Cases for the Validation of CFD Codes*, AGARD-AR-303 Vol. II, August 1994, pp. B4.1-B4.21.

⁶Redeker, G., Muller, R., Ashill, P. R., Elsenaar, A., and Schmitt, V., "Experiments on the DLR-F4 Wing Body Configuration in Several European Wind Tunnels," in Chapter 2 of *Aerodynamic Data Accuracy and Quality: Requirements and Capabilities in Wind Tunnel Testing*, AGARD-CP-429, July 1988.

⁷Elsholz, E., "The DLR-F4 Wing/Body Configuration," in *ECARP - European Computational Aerodynamics Research Project: Validation of Turbulence Models, Notes on Numerical Fluid Mechanics*, Vol. 58, 1997, pp. 429-450.

⁸Brodersen, O., and Sturmer, A., "Drag Prediction of Engine-Airframe Interference Effects Using Unstructured Navier-Stokes Calculations," AIAA Paper 2001-2414, June 2001.

⁹Vassberg, J. C., Sclafani, A. J., and DeHaan, M. A., "A Wing-Body Fairing Design for the DLR-F6 Model: a DPW-III Case Study," AIAA Paper 2005-4730, June 2005.

¹⁰Vassberg, J. C., Tinoco, E. N., Mani, M., Brodersen, O. P., Eisfeld, B., Wahls, R. A., Morrison, J. H., Zickuhr, T., Laflin, K. R., and Mavriplis, D. J., "Summary of the Third AIAA CFD Drag Prediction Workshop," AIAA Paper 2007-0260, January 2007.

¹¹Tinoco, E. N., Winkler, C., Mani, M., and Venkatakrishnan, V., "Structured and Unstructured Solvers for the 3rd CFD Drag Prediction Workshop," AIAA Paper 2007-0255, January 2007.

¹²Mavriplis, D. J., "Results from the 3rd Drag Prediction Workshop using the NSU3D Unstructured Mesh Solver," AIAA Paper 2007-0256, January 2007.

¹³Sclafani, A. J., Vassberg, J. C., Harrison, N. A., DeHaan, M. A., Rumsey, C. L., Rivers, S. M., and Morrison, J. H., "Drag Predictions for the DLR-F6 Wing/Body and DPW Wings Using CFL3D and OVERFLOW on an Overset Mesh," AIAA Paper 2007-0257, January 2007..

¹⁴Brodersen, O., Eisfeld, B., Raddatz, J., and Frohnapfel, P., "DLR Results from the Third AIAA CFD Drag Prediction Workshop," AIAA Paper 2007-0259, January 2007.

¹⁵Anon., *U.S. Guide to the Expression of Uncertainty in Measurement*, ANSI/NCSL Z540.2-1997, October 1997.

¹⁶Salas, M. D., "Digital Flight: The Last CFD Aeronautical Grand Challenge," *Journal of Scientific Computing*, Vol. 28, Nos. 2/3, 2006, pp. 479-505.

¹⁷Salas, M. D., "Some Observations on Grid Convergence," *Computers & Fluids*, Vol. 35, No. 7, 2006, pp. 688-692.

¹⁸Spalart, P. R., and Allmaras, S. R., "A One-Equation Turbulence Model for Aerodynamic Flows," *La Recherche Aerospatiale*, No. 1, 1994, pp. 5-21.

¹⁹Wheeler, D. J., *Advanced Topics in Statistical Process Control*, SPC Press, Knoxville, TN, 1995.